ELSEVIER

Journal of Electron Spectroscopy and Related Phenomena 84 (1997) 231–250

JOURNAL OF
ELECTRON SPECTROSCOPY
and Related Phenomena

SMART: a planned ultrahigh-resolution spectromicroscope for BESSY II

R. Fink[a,*], M.R. Weiss[a], E. Umbach[1a], D. Preikszas[b], H. Rose[b], R. Spehr[b], P. Hartel[b], W. Engel[c], R. Degenhardt[c], R. Wichtendahl[c], H. Kuhlenbeck[c], W. Erlebach[c], K. Ihmann[c], R. Schlögl[c], H.-J. Freund[c], A.M. Bradshaw[c], G. Lilienkamp[d], Th. Schmidt[d], E. Bauer[d], G. Benner[e]

[a]*Universität Würzburg, Experimentelle Physik II, Am Hubland, D-97074 Würzburg, Germany*
[b]*Technische Hochschule Darmstadt, Angewandte Physik, Hochschulstraße 6, D-64289 Darmstadt, Germany*
[c]*Fritz-Haber-Institut der Max-Planck-Gesellschaft, Faradayweg 4–6, D-14195 Berlin, Germany*
[d]*Technische Universität Clausthal, Leibnizstr. 4, D-38678 Clausthal-Zellerfeld, Germany*
[e]*LEO Elektronenmikroskopie GmbH, D-73446 Oberkochen, Germany*

Received 19 June 1996; accepted 2 January 1997

Abstract

A new UHV spectromicroscope called SMART (spectromicroscope for all relevant techniques) is currently under construction for a soft X-ray undulator beamline at BESSY II. The instrument consists of a plane-grating monochromator with an aspherical focusing mirror and an ultrahigh-resolution, low-energy electron microscope containing an energy filter. It can be used as a photoemission microscope for a variety of electron spectroscopies (XAS, XPS, UPS, XAES) and has a calculated spatial resolution of better than 1 nm. A maximum energy resolution of about 0.1 eV will be provided by a corrected omega filter. The high lateral resolution of the electron microscope will be achieved through the correction of the chromatic and spherical aberrations of the objective lens by means of an electrostatic mirror in combination with a corrected magnetic beam separator. An additional electron source placed on the other side of the beam separator opposite the electrostatic mirror will also allow LEEM, MEM and small-spot LEED investigations to be carried out. The basic ideas, the various modes of operation and the electron optical design of the instrument are outlined. © 1997 Elsevier Science B.V.

Keywords: SMART; Ultrahigh-resolution spectromicroscope; XPEEM; LEEM; Small-spot LEED

---

1. Introduction

The visualization of structures on an atomic scale is an important and ongoing task of microscopy. Using the techniques of high-resolution electron microscopy and scanning tunnelling microscopy a spatial resolution in the subnanometer range can be achieved and utilized both in solid state research and materials science as well as in biology and medicine. In many cases, however, spectroscopic information is also needed to understand fully the various chemical and physical processes involved. For the last 20 years enormous efforts have been made in many laboratories to develop spectroscopic methods for use in

---

[*] Corresponding author. Tel.: +49 9318 885163; fax: +49 9318 885158; e-mail: raifi@physik.uni-wuerzburg.de

[1] Project coordinator.

0368-2048/97/$17.00 © 1997 Elsevier Science B.V. All rights reserved
PII S0368-2048(97)00016-9

electron microscopes (see for example [1]). In transmission microscopy, electron energy-loss spectroscopy (EELS), as well as X-ray emission spectroscopy, is now well established. In the case of EELS these efforts have culminated in the development of the imaging omega filter which has been fully corrected to second order.

In surface studies this problem has been partly overcome using scanning Auger microscopy, which employs a focused electron beam of several 10 keV kinetic energy to excite element-specific Auger electrons at a lateral resolution of the order of 50 nm (see for example [2]). There are, however, several serious drawbacks to the latter method, such as radiation damage, low signal-to-background and signal-to-noise ratios, and poor sensitivity to different chemical states of a given element. These problems can be solved to a large extent by using photoelectron spectroscopy or photoemission. Since the development of photoemission as a tool in surface analysis, considerable effort has also been made in combining spectroscopic information with lateral resolution. Only in the past 10 years has significant progress been made, in particular since the construction of dedicated synchrotron radiation sources which provide a high photon flux in the UV and soft X-ray ranges. The tunability and polarization of synchrotron light also allows near-edge photoabsorption experiments (NEXAFS/XANES) to be performed. Moreover, photoelectron spectra can be measured near the threshold, where the photoionization cross-section is highest, or 40–100 eV above where the surface sensitivity is highest. Finally, the energy resolution can be sufficiently high that elemental and even chemical state mapping is possible.

Two types of photoemission microscope have been installed at various synchrotron radiation sources, namely scanning and imaging instruments. In scanning microscopy the lateral resolution is determined by the size of the irradiated spot at the surface (''microspectroscopy''), whereas in the imaging technique (''spectromicroscopy'') the resolution is determined by the aberrations of the electron-optical imaging system consisting of electrostatic and/or magnetic lenses. The latter technique avoids the problem of focusing soft X-rays down to ultrasmall spot sizes, the required lateral dimensions of which are in any case below the diffraction limit. In addition, an instrument in which the image is formed by a parallel collection of information is, in general, more efficient than one in which the image is constructed in a serial way. Setting up a high-resolution spectromicroscope requires, however, a detailed consideration of the electron optics. In addition, the high-voltage equipment and stabilized power supplies for the electrostatic/magnetic lenses require considerable capital expenditure.

For the investigation of rough surfaces (e.g. polycrystalline samples) scanning microscopy has certain advantages over the imaging technique since high electric fields (about 10^5 V cm^{-1} at the sample surface) are usually employed for the latter and cusps at the surface lead to a significant field perturbation. This restriction can be partly overcome by imaging in a mode which keeps the sample field-free. In general, mechanical and thermal stability plays an important role in all photoelectron microscopes if the spatial resolution is to be reduced to several tens of nanometres. Apart from the need to reduce the size of the illuminated spot or to correct electron optical components, the stability requirement is at present one of the main obstacles in reaching ultrahigh spatial resolution.

Most of the instruments at present in use are described in other articles in this volume and will therefore not be discussed here. We briefly note that the highest spatial resolution in a microspectroscope (100 nm) has been obtained by Ade et al. [3] with their Fresnel zone plate instrument SPEM on the Brookhaven X1A undulator beamline. Several spectromicroscopes have so far been used at synchrotron radiation sources. The highest spatial resolution (40 nm) [4,5] has recently been achieved by the Clausthal group at BESSY I using the Bauer LEEM/PEEM instrument [6] in the photoemission mode. This was the first microscope at a synchrotron radiation source to be equipped with a band pass energy filter. Tonner and co-workers have employed a relatively simple device from the electron optical point of view to record images at a lateral resolution of about 2 μm both at Aladdin in Wisconsin [7] and at the Advanced Light Source (ALS), Berkeley [8] where another instrument with a band pass filter called PRISM has recently gone into operation [9]. The PEEM of Engel et al. [10] has been used by Kisker and co-workers to image magnetic domains [11].

Another microscope by Schönhense and co-workers has been used at BESSY I, although details have not been published yet.

Further improvements in spatial resolution and energy resolution can be expected in the next few years with the new high-brilliance third-generation synchrotron radiation sources. Dedicated microspectroscopy beamlines are in operation or under construction at the ALS, Berkeley, and at ELETTRA, Trieste, Italy. Most of the planned instruments are of the microspectroscope type. At ELETTRA the SuperMAXIMUM project aims for a lateral resolution of about 50 nm [12], and the MEPHISTO microscope plans to reach 20 nm in the XANES mode [13]. At the ALS the SpectroMicroscopy beamline 7.0 will be equipped with several microscopes [8]. In addition, a new beamline (7.3.1) dedicated to magnetic microscopy is presently under construction [14]. For most instruments, however, optimum performance is limited to certain photon energies because of the use of zone plates or of multilayer mirrors in a Schwarzschild objective, and only one mode of operation is possible. In zone-plate microspectroscopes, for example, the tunable energy range is restricted to about 15% of the chosen photon energy with a rather large photon energy bandwidth.

These limitations can be overcome by the combination of a high-flux, high-resolution monochromator with a high-resolution electron microscope fitted with an imaging energy filter. Various spectroscopies, spectroscopic imaging modes and diffraction techniques then become possible thus leading to the name of the instrument (SMART = Spectromicroscope for All Relevant Techniques). Six groups from different universities, research institutes and industry have recently started to construct such a versatile spectromicroscope for a soft X-ray undulator at BESSY II. Although the calculated resolution limit is below 1 nm, the aim is a lateral resolution of about 2 nm and an energy resolution of 0.1 eV. High photon flux at the sample surface is achieved with an aspherical refocussing mirror which demagnifies the monochromator exit slit. The significant increase in spatial resolution results primarily from the correction of the spherical and chromatic aberrations of the objective lens. We note that a photoemission microscope with a mirror corrector has also been realized by Skoczylas et al. [15]. The chromatic aberration of this instrument is corrected experimentally by means of an electrostatic mirror [16]. Very recently, the simultaneous correction of chromatic and spherical aberrations has also been achieved [17]. Our instrument can also be operated as a low-energy electron microscope (LEEM) which, in addition, allows mirror electron microscopy (MEM) and small-spot LEED to be performed [5,14]. To our knowledge this is the most ambitious project in the field of spectromicroscopy at present and should open up new fields in basic and applied research when the instrument reaches its ultimate resolution.

In this paper we describe the general concept in Section 2 and the various modes of operation in Section 3. A more detailed description of the electron optical components is given in Section 4.

2. General concept

A schematic overview of the instrument is shown in Fig. 1. At the current state of planning the instrument will go on the U49 undulator shortly after the commencement of operations at BESSY II in 1998. A plane-grating, grazing-incidence monochromator with the designation PM-6 will provide soft X-radiation in the spectral range from about 20 to 2000 eV with a maximum spectral resolving power of $h\nu/\Delta h\nu \approx 10^4$. The exit slit of the monochromator is focused on the sample surface by an ellipsoidal grazing-incidence mirror yielding a spot of about $5 \times 10\ \mu m^2$. The monochromator and focusing mirror are the responsibility of the groups in Würzburg and Berlin.

The experimental chamber, sample transfer and manipulator will be constructed by the Clausthal group in collaboration with the group in Würzburg. The design of the manipulator is particularly critical since the sample position must be stable to within 1 nm, including the allowance for the effect of thermal drifts. In addition, an xy-movement of about 5 mm is necessary so that the surface of the whole sample can be investigated. The reproducibility of this movement should be considerably better than 1 μm. For reaching these specifications the experience obtained with the series of Bauer LEEM/PEEM instruments will be invaluable [18].

The objective lens consists of a UHV-compatible electrostatic immersion lens with a superimposed

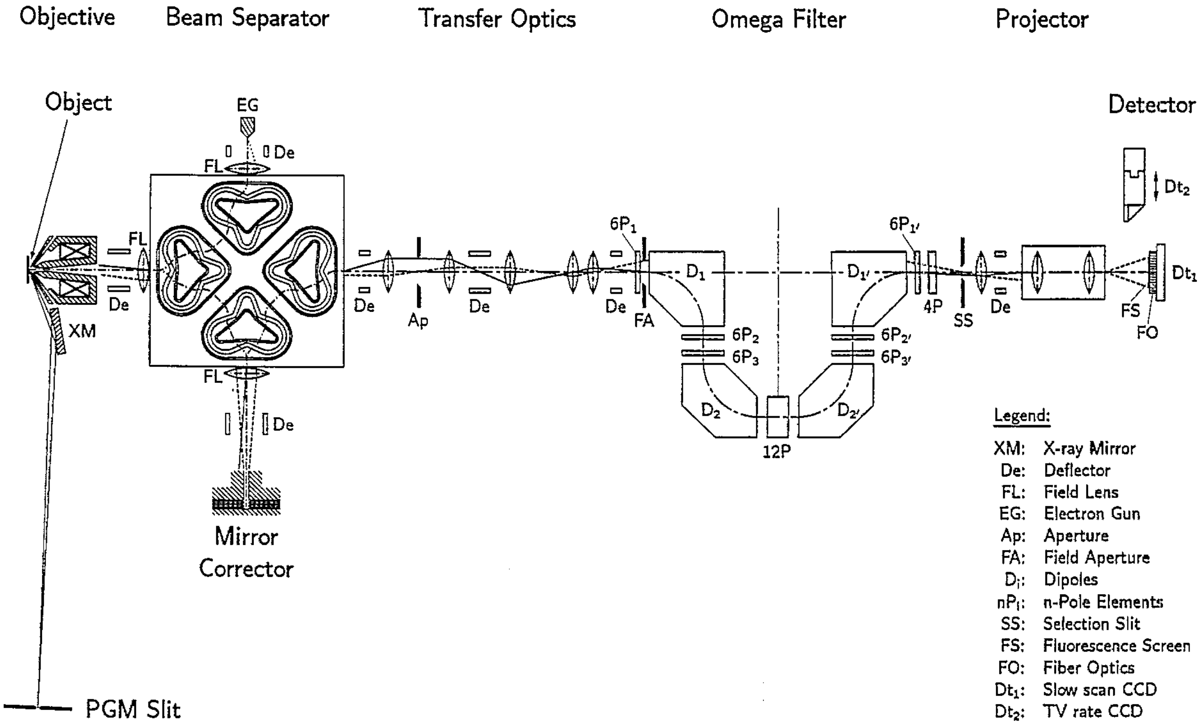

Fig. 1. Schematic layout of the new spectromicroscope SMART under construction for a BESSY II undulator beamline.

magnetic field, a stigmator and deflection elements. The lens will be built by LEO (formerly Zeiss electron optics) and installed completely in the sample chamber which is separated from the beam separator chamber by an all-metal valve. Detailed calculations for the final layout of the objective lens system are currently being performed in Darmstadt.

The key factor in reaching the unprecedented spatial resolution is a beam separator combined with an electrostatic tetrode mirror which corrects the spherical and chromatic aberrations of the objective lens. The beam separator designed by Rose and Preikszas [19] is a complex, highly symmetric configuration of different magnetic dipole fields and has been optimized for the present instrument. Its fourfold symmetric form allows an electron gun with field emission source and condenser system to be placed opposite to the tetrode mirror, so that the microscope can also be operated in the LEEM, MEM and small-spot LEED modes. The detailed design and construction is being carried out in Darmstadt. In the early stages of the project an intermediate lens will replace the beam separator and the electrostatic mirror, since these elements require considerable development work and will be ready approximately two years after the other components.

After the beam separator a transfer system follows consisting of five electrostatic einzel lenses. This forms a magnified image of the sample and a demagnified image of the diffraction pattern at two different positions in front of the imaging electron energy analyzer. The latter is a so-called omega filter, a suitable version of which with the required electron optical properties has already been built for a 100 keV transmission electron microscope at the Fritz-Haber-Institut [20]. The filter consists of an omega-shaped configuration of dipole magnets which serves as an energy discriminator for photoelectrons and (in the LEEM mode) for inelastically scattered and secondary electrons. Sextupole magnets are used for correction purposes. The detailed design is based on the earlier version by Krahl and on the calculations by Lanio et al. [20]. The aberrations have been corrected up to second order which has not been the case for other energy filters constructed to date. The low electron energy of 15 keV in the present instrument leads to a relatively high dispersion of 35 μm eV^{-1} which should make it possible to work at an energy resolution of 0.1–0.2 eV in an energy window of 35 eV. In addition to normal two-dimensional imaging, parallel detection in this energy window is also possible by imaging the dispersion plane of the omega filter onto the detector. The projection system consists of three einzel lenses which allow a variable magnification (20–150) and transfer the dispersion plane or the image behind the filter onto the two-dimensional detector. This group of components will be realized at the Fritz-Haber-Institut where the final assembly of the complete instrument will also take place.

3. Modes of operation

The various modes of operation include both microscopy and spectroscopy as well as low-energy electron diffraction; in all cases the pass energy of the omega filter is kept constant because a change of the excitation of its dipole magnets requires a readjustment of all multipole correctors and realignment. Setting up the instrument therefore begins with the appropriate excitation of the omega filter which determines the pass energy E (see Fig. 2). The acceleration voltage U applied between sample (cathode) and anode then determines the initial kinetic energy $E_0 = E - eU$ of the electrons at the sample surface which can pass through the omega filter and form the image. E_0 can be varied between 0 and 1500 eV and, in general, should be kept constant during an experiment because a change of E_0 requires refocussing of the objective lens and a readjustment of the mirror corrector. Some exceptions will be discussed later. A slit in the dispersion plane of the omega filter defines an energy window ΔE which can be set between 0.1 and 5 eV. The various modes of operation are described briefly in the next sections.

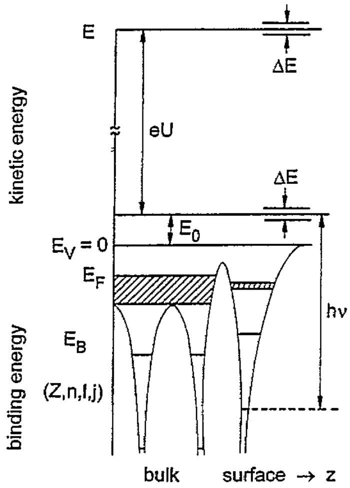

Fig. 2. Schematic energy level diagram for the spectromicroscope: E, pass energy; ΔE, energy window; E_0, initial energy; U, accelerating voltage; E_B, binding energy; $h\nu$, photon energy; E_F, Fermi level; E_V, vacuum level.

3.1. High-resolution microscopy with electrons of selected energy

Theory predicts a lateral resolution of less than 1 nm if the mirror corrector is in operation and if the width in the energy distribution of the electrons forming the image is less than 5 eV.

3.1.1. Photoelectron emission microscopy (PEEM)

The undulator beamline provides monochromatized photons in the energy range of 20 to 2000 eV. Thus valence electrons as well as core electrons can be excited. In addition, the microscope will be equipped with a conventional UV light source that provides photons with energies up to 7 eV, so that PEEM can also be performed in its traditional form as a threshold microscopy. In this mode the technique is extremely sensitive to small differences in the local work function and has been used in recent years for investigations of heterogeneous reactions [21–24] and diffusion phenomena [25], at solid surfaces as well as of biological samples [26].

The excitation of core electrons is of particular interest because it provides a chemical contrast mechanism. There are three different ways of imaging the distribution of a particular element, i.e. to perform elemental mapping. First, core electrons of the element of interest with binding energy E_B can be used. The photon energy $h\nu$ has to be set within the interval $E_0 + E_B - \Delta E/2 < h\nu < E_0 + E_B + \Delta E/2$. Optimally, E_0 should be within the energy range of about 30 to 100 eV for several reasons: (i) E_0 is then beyond the large peak of secondary electrons which considerably improves the signal-to-background ratio.

(ii) At photon energies near the ionization threshold the cross-section for exciting the core electron is close to its maximum. (iii) The experiment is very surface sensitive because the mean free path for inelastic scattering of electrons is rather small in this kinetic energy range. (iv) The transmission of the objective lens, which decreases with increasing E_0, is still reasonably high. Second, Auger electrons characteristic of the element or compound of interest are imaged by adjusting E_0 to the corresponding kinetic energy E_A of the Auger electron. A considerably higher photon bandwidth can be used in this mode, thus increasing the photon flux density at the sample surface. The method is also very surface sensitive. Third, secondary electrons can also be used for elemental mapping by taking advantage of the fact that the intensity of secondaries rises steeply when the slowly increasing photon energy exceeds the excitation threshold of a particular core level. Contrast is strongly increased if two images at slightly different photon energies, one above and the other below the threshold, are taken and the difference is plotted. In order to obtain high intensities, an E_0 value at the intensity maximum of the secondaries between 2 and 3 eV is selected. In contrast to the photoelectron and Auger modes, bulk information is also obtained because excited atoms in deeper layers contribute substantially to the emission of secondary electrons. This mode of imaging has been performed successfully using simple photoemission microscopes that do not have an imaging filter [27]. An aperture in the back focal plane of the objective lens provides sufficient energy filtering for a lateral resolution of about 1 μm. Magnetic structures, for example, have been imaged by these instruments using polarized synchrotron radiation [11].

In spite of the extremely high photon flux densities available at BESSY II, lack of intensity will limit the achievable lateral resolution in many applications. The correction of the spherical and chromatic aberrations is thus of great importance in this context, because it allows much larger acceptance angles, a broader energy distribution of the electrons forming the image, and hence a considerable increase in transmission (up to two orders of magnitude).

3.1.2. Low-energy electron reflection microscopy (LEEM)

The electron gun at the beam separator provides a beam of electrons the kinetic energy of which is equal to the pass energy E. In this case E_0 is the kinetic energy of the incident electrons at the sample surface. The omega filter eliminates all inelastically scattered and secondary electrons. Hence the image is formed solely by elastically scattered electrons. The achievable lateral resolution should approach the theoretical resolution limit because intensity problems are not expected in this mode.

3.1.3. Mirror electron microscopy (MEM)

In order to perform MEM the acceleration energy eU has to be somewhat larger than the beam energy E. Electrons are then reflected at an equipotential surface in front of the sample surface. MEM is particularly sensitive to the topography and to electrical and magnetic microfields at the surface, as recent investigations of heterogeneous reactions, for example, have shown [28]. The interpretation of images obtained from rough surfaces is, however, difficult and sometimes impossible.

3.1.4. Special imaging mode for PEEM and LEEM in the case of rough sample surfaces

In general, in emission microscopes a strong electric field is applied at the sample surface with the field vector parallel to the optic axis. Field components perpendicular to the optic axis due to the topography of the surface and contact potentials cause distortions of the electron trajectories and thus give rise to a so-called topography and microfield contrast which may be useful. The effect can, however, destroy the image if the surface is too rough. The proposed cathode lens can handle the problem of rough surfaces in the PEEM and LEEM mode because it allows the electrical field strength at the sample surface to be reduced to zero. However, E_0 should not be smaller than 500 eV in this mode in order to maintain the very high lateral resolution.

3.2. Spectroscopy in the microscopy mode

In this mode of operation a magnified image of the sample is always produced at the final image detector. The pass energy E of the omega filter and the initial kinetic energy E_0 that is accepted by the optics are fixed, while the photon energy $h\nu$ is tuned in steps through the energy range of interest and an image is recorded after each step. In this way spectra are recorded simultaneously for all picture elements the size of which can be as small as 1×1 nm^2, if sufficient intensity is available. In many cases, however, recording of spectra from some specific areas of interest will be sufficient. Number, position and size of these areas can be selected by the detector system. Because the final state energy of the recorded electrons is fixed, this mode is often referred to as constant final state (CFS) spectroscopy.

3.2.1. Photoelectron spectroscopy in the constant final state mode

Photoelectron spectroscopy in both the valence and the core level regions can be performed in this mode. The energy resolution results from a convolution of the transfer functions of both the X-ray monochromator and the omega filter. The latter, however, effectively determines the resolution limit of about 0.1 eV, at least in the low photon energy range.

3.2.2. Chemical analysis with high surface sensitivity

The analysis is based on the spectroscopy of core electrons; the optimal settings for E_0 have already been discussed in Section 3.1.1. For a survey scan, the photon energy is now tuned, for example from E_0 to 2000 eV, causing a brightening in the image at the location of elements when the energy condition for the emission of a particular core electron is fulfilled. The binding energies of all constituent elements with $E_B < 2000 \text{ eV} - E_0$ can be identified in this way. A detailed discussion of the detectability of small amounts of a particular element on a solid surface and other quantities characterizing the sensitivity of the chemical analysis would be too long here, and we refer to a paper of Bauer [29]. A more detailed analysis of the chemical states of a particular element can be performed by a photon energy scan on expanded scale just around $E_B + E_0$.

3.2.3. X-ray absorption spectroscopy

X-ray absorption spectroscopy at a surface (XANES, NEXAFS, SEXAFS) is performed by recording the signal of a secondary effect (e.g. secondary electron or Auger emission) induced by the primary core electron excitation while the photon energy is tuned through the energy range of interest. In the case of secondary electrons, E_0 will be set at the intensity maximum of secondaries between about 2 and 3 eV as has already been discussed in Section 3.1.1. By tuning the photon energy through the available range a chemical analysis can also be performed. The surface sensitivity attainable with the method described in Section 3.2.2 is, however, lost because excited core electrons of deeper lying atoms make a large contribution to secondary electron emission, as mentioned above. Micro-XANES measurements with secondary electrons were first performed by Harp and Tonner [7]. A significantly improved signal-to-noise ratio and an increase in the surface sensitivity are achieved when E_0 corresponds to an Auger transition in the element or compound of interest.

It should be noted that the energy resolution in the X-ray absorption spectroscopy mode is solely determined by the energy resolution of the X-ray monochromator. The energy window of the omega filter is thus a parameter that can be varied in order to optimize the imaging conditions which, in general, will involve a trade-off between contrast, intensity and resolution.

3.2.4. Conventional photoelectron spectroscopy

Electron spectroscopy in the classical sense (ESCA and AES) using photons with fixed energy is also possible in the microscopy mode if E_0 is tuned through the energy range of interest and automatic refocussing of the image is performed. The aberration corrector, however, complicates matters because refocussing includes a readjustment of the corrector. This kind of spectroscopy will be practicable only if refocussing and readjustment of the aberration corrector are completely computer-controlled.

3.2.5. Photoelectron spectroscopy in the constant initial state (CIS) mode

In a computer-controlled instrument it is straightforward to record images while both E_0 and $h\nu$ are tuned stepwise in such a way that $h\nu - E_0 = E_B$ remains constant, that is the excited initial state remains the same.

3.3. Electron spectroscopy of selected small sample areas

In this mode the dispersive plane of the source image at the omega filter, that is the spectrum rather than the sample image, is projected onto the final image detector which allows parallel recording of the spectrum. The omega filter performs stigmatic imaging which, however, is not desired in this particular case. By the appropriate excitation of a quadrupole focusing only in the dispersive direction can be achieved. A line spectrum is produced which distributes the intensities collected in the various energy channels over a large number of pixels in the CCD detector thus enlarging the detectable dynamic signal range. The lateral resolution of the detector δx, projector magnification M_P and dispersion D of the omega filter determine the energy resolution: $\delta E = \delta x / M_P \cdot D$. With $D=35$ μm eV^{-1} and $\delta x=70$ μm, $\delta E = 2$ eV$/M_P$ is obtained. Thus for $M_P < 20$ the lateral resolution of the detector determines the spectroscopic resolution; for $M_P > 20$, however, aberrations of the omega filter play a role and limit the ultimate energy resolution to a value somewhat smaller than 0.1 eV. A more detailed discussion is given in Section 4. Note that a real slit is not needed in this mode, although a broad energy window corresponding to about 35 eV which can be positioned within the energy range 0 to 1500 eV is used to reduce the background due to stray electrons. This corresponds to the largest window that can be transferred through the aberration corrector. Sample areas of interest are selected by the field aperture at the entrance of the omega filter. The smallest selectable sample area is about 5 nm in diameter.

3.4. Low-energy electron diffraction (LEED)

In order to perform LEED the transfer optics project the source image of the electron gun rather than the sample image onto the entrance plane in front of the omega filter. Thus an energetically filtered diffraction pattern which is free of secondary and inelastically scattered electrons is projected onto the final image detector. Selectable apertures in the electron gun system allow the size of the illuminated sample area to be controlled; it can be made as small as 1 μm. Thus small-spot LEED experiments can also be performed.

4. Description of major components

Since some of the components in the electron optics of this new spectromicroscope are being constructed for the first time in an instrument of this type, we will concentrate on these features in the following more detailed description.

4.1. Photon source: the PM-6 monochromator

The new instrument will be installed on a U49 undulator at BESSY II with 81 periods of 49 mm length. At 1.7 GeV storage ring energy, the first harmonic can be varied in the range from 136 to 497 eV for an undulator gap of 16 mm to open [30]. A plane-grating grazing-incidence monochromator with the designation PM-6 will provide soft X-radiation in the spectral range from about 20 to 2000 eV. This instrument may be regarded as a further development of Petersen's SX 700 monochromator [31] and has a maximum spectral resolving power of $h\nu/\Delta h\nu \approx 10^4$. A gold-covered ellipsoidal grazing-incidence mirror with an incident angle of 2° and a demagnification ratio of about 10:1 is then used to focus the 50 μm × 50 μm exit slit of the monochromator down to a spot of about 5 μm × 10 μm on the sample surface. This refocussing mirror is rigidly mounted in the experimental chamber with a distance of about 10 cm to the sample. The same principle for spot size reduction has recently been realized in the PISAM-II instrument by the Würzburg group [32]. At a photon energy of 400 eV and a spectral resolution of 60 meV, the flux is estimated to be about 2×10^9 photons μm^{-2} s^{-1}. The use of an interchangeable monochromator grating with 360 lines mm^{-1} (as compared to 1200 lines mm^{-1} for the high-resolution mode) increases the photon flux by a factor of four at the expense of energy resolution.

4.2. Sample handling

Samples with a diameter between 10 and 14 mm will be mounted on a transferable sample holder with a heater and a W/WRe thermocouple, allowing sample temperatures to be set between 200 and 2300 K. The sample holder is fixed to a high precision *xyz*-manipulator by a specially designed clamp mechanism. Positioning of the sample within an *xy*-range of ± 5 mm in front of the objective lens can be performed with a reproducibility of better than 1 μm and monitored with a digital length scale system mounted on the manipulator. An additional tilt mechanism allows the surface normal to be adjusted precisely along the symmetry axis of the objective lens. Cooling the sample to about 200 K is achieved with a copper braid connected to a liquid nitrogen reservoir fitted to the manipulator. The sample bias of 15 kV is connected via a separate high-voltage feedthrough to the insulated sample holder. The manipulator is installed in a specially designed experimental chamber which also houses the refocussing mirror (Section 4.1) and the objective lens (Section 4.4) as well as various effusion cells for metals and semiconductors and a gas dosing system for in situ microscopy and photoemission experiments.

4.3. Sample preparation

For extensive sample preparation a separate UHV chamber will be mounted on the spectromicroscope. It allows for sputtering, heating, and for preparation of ultrathin films of metals, semiconductors and organic materials. Gas exposure is monitored by a quadrupole mass spectrometer. Conventional surface analysis during preparation can be performed with a four-grid LEED-Auger system. A fast entry load-lock for quick sample introduction is connected to the preparation chamber.

4.4. Objective lens

Photoelectrons are emitted from the sample surface into the full half space. If X-rays are used for excitation, the photoelectron energy distribution is rather broad. Imaging of all these electrons would not be advisable because in this case the aberrations of the objective lens strongly reduce both contrast and resolution. In order to achieve the conditions of Gaussian optics, an aperture stop which confines the beam to the paraxial region and an imaging filter that selects electrons within an energy range $\Delta E < E_0$ are necessary. Since these measures reduce drastically the number of electrons contributing to image formation, the transmission of such a microscope would be rather low. To increase the transmission, the spherical and the chromatic aberrations must be eliminated or significantly reduced. At the same time these corrections improve the lateral resolution. The importance of both lateral resolution and transmission for photoemission microscopy has been emphasized by Bauer [29] who has used these two quantities to define a quality factor.

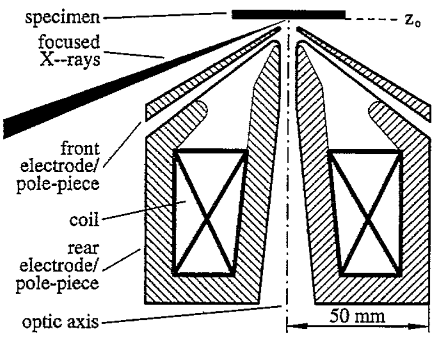

Fig. 3. Scheme of the rotationally symmetric objective lens. Two electrode surfaces enclose the magnetic pole pieces; the sample holder serves as the third electrode.

A simple and effective reduction of the aberration coefficients is obtained if a strong electric field is applied to the sample surface. For this traditional approach the sample becomes the cathode of an immersion lens. The strong accelerating field puts severe constraints on the shape and flatness of the sample which cannot be met in many cases. We have therefore developed an immersion objective lens (Fig. 3) which can operate with varying electric field strength at the sample surface. For this objective lens the aberrations remain sufficiently small for all modes of operation. The remaining axial aberrations can be compensated by those of a mirror corrector, which represents an additional step of improvement. Electrons leave the immersion objective lens with the pass energy $E = 15$ keV $\gg E_0$ regardless of the chosen mode of operation. For each mode, however, the objective lens must be adjusted in such a way that its image plane remains fixed. This condition can be fulfilled by means of a magnetic field.

The constant of the electrostatic potential is chosen in such a way that the initial kinetic energy of the image-forming electrons corresponds to the object potential φ_0, i.e. $E_0 = e \cdot \varphi_0$. The electric field at the surface of the sample can be adjusted by means of the potential applied to the first electrode. The conical shape of this electrode allows the sample to be illuminated by the focused X-ray beam. The rear electrode is put at the column potential (15 kV). Both electrodes serve simultaneously as pole pieces for the superimposed magnetic field. The front pole

Table 1
Intermediate magnification M, chromatic aberration coefficient C_C and spherical aberration coefficient C_S of the objective lens for various modes of operation. The aberration constants C_C and C_S refer to the image plane, whereas $\tilde{C}_C$ and $\tilde{C}_S$ refer to the object plane

φ_0/V	φ'_0/kV mm^{-1}	$\tilde{C}_C/\mu$m	$\tilde{C}_S/\mu$m	M	C_C/m	C_S/km
500	0	1235	1880	16.7	7.7	24.5
1000	0	1539	2550	16.5	24.9	11.27
2000	0	1984	3920	17.1	12.16	7.03
5000	0	3070	8040	19.0	5.82	5.48
20	1	19.32	27.1	11.7	55.3	10.56
50	1	47.1	74.9	12.0	36.1	8.26
100	1	91.5	162.2	12.4	26.2	7.11
200	1	174.7	349	12.9	19.16	6.32
500	1	397	932	13.8	12.66	5.65
1000	1	713	1893	14.8	9.23	5.35
2000	1	1243	3690	16.1	6.74	5.18
5000	1	2520	8270	18.5	4.54	5.09
1	5	0.205	0.276	12.7	62.0	13.53
2	5	0.413	0.614	12.7	44.5	10.75
5	5	1.050	1.833	12.8	28.9	8.29
10	5	2.14	4.31	12.9	21.1	7.05
20	5	4.39	10.37	13.0	15.56	6.19
50	5	11.52	33.9	13.2	10.64	5.45
100	5	24.2	83.5	13.4	9.18	5.09
200	5	51.3	205	13.8	6.44	4.86
500	5	140.9	650	14.4	4.91	4.70
1000	5	304	1487	15.2	4.15	4.66
2000	5	654	3210	16.2	3.61	4.67
5000	5	1745	7820	18.4	3.10	14.69

piece is placed close to the sample, a location which is favourable for producing the necessary refractive power without introducing large aberrations.

In Table 1 the intermediate magnification and the aberration coefficients are listed for various modes of operation defined by the potential $\varphi = \varphi_0$ and the axial electric field strength φ_0' at the object plane $z = z_0$. At $\varphi_0' = 5$ kV mm^{-1} the object potential can be lowered to 1 V. Operational modes with a negligibly small electric field at the surface of the specimen are possible for object potentials larger than about 500 V. For smaller potentials the aberrations become unduly large and cannot be corrected by the mirror.

4.5. Aberration corrections

4.5.1. Arrangement

According to the Scherzer theorem [33] spherical and chromatic aberrations of rotationally symmetric lenses are unavoidable. In particular, the refracting power is always larger in the outer zones than in the inner region of a round lens, and electrons with a higher kinetic energy are always less strongly focused than electrons with a lower energy. Electrostatic electron mirrors are well suited for eliminating simultaneously the spherical and the chromatic aberrations of round lenses [34]. The compensating aberrations of the mirror are adjustable if the mirror consists of four electrodes. The successful application of such a mirror depends on an appropriate beam separator which separates the incoming ray from the reflected ray without introducing dispersion or second-order aberrations. We will therefore use a corrector consisting of a tetrode mirror and a highly symmetric magnetic beam separator. Due to this symmetry the aberrations of the beam separator cancel out after each passage through one of its quadrants.

The arrangement of the corrected imaging system is shown in Fig. 4. Electrons emitted from the sample surface are accelerated by the immersion objective lens (see Fig. 3) and form an intermediate image in front of the beam separator. The chromatic and the spherical aberrations of the objective lens blur the first and second intermediate images which are located at

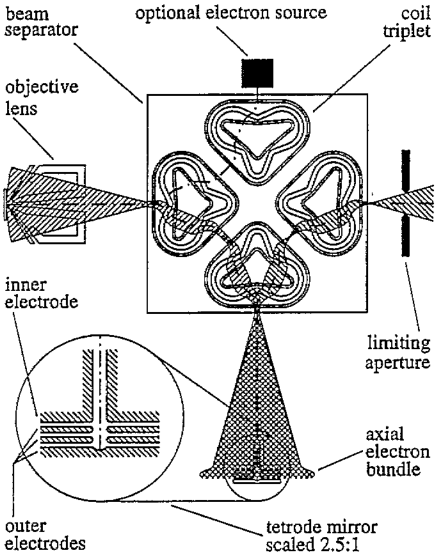

Fig. 4. Corrected imaging system consisting of an electromagnetic immersion lens, a twofold-symmetric beam separator and a tetrode mirror. The beam-limiting aperture is shown enlarged.

the boundaries of the beam separator facing the objective lens and the mirror, respectively. After the first passage through the beam separator the electrons are reflected by the tetrode mirror which simultaneously compensates for the chromatic and the spherical aberrations of the objective lens. At the end of the subsequent second passage the electron bundle forms an image with negligibly small aberrations at the exit plane (before the limiting aperture) of the beam separator. By the installation of an electron source at the other side of the beam separator (see Fig. 4), one can alternatively illuminate the object with electrons [20].

4.5.2. Beam separator

The beam separator consists of two quadratic plane pole plates separated from each other by a distance of 7 mm. Four coil triplets are placed into grooves on the inner surface of each pole piece, as shown in Fig. 5. The currents $I_1 = I$, $I_2 = -2I$ and $I_3 = I$ of each coil triplet produce two regions with opposite magnetic field B and $-B$, respectively. Each of the grooves contains a main coil and two adjacent tuning coils. The inner and the outer tuning coils can be excited independently for aligning precisely the required path of rays.

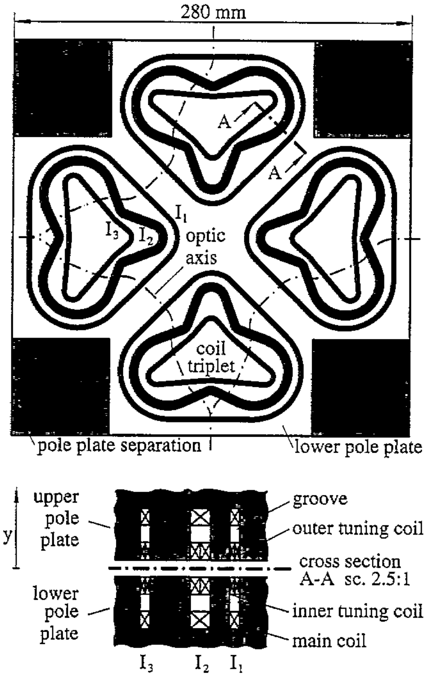

Fig. 5. Midsection view of the beam separator and the vertical cross-section A–A. The direction of the y coordinate is perpendicular to the pole plates.

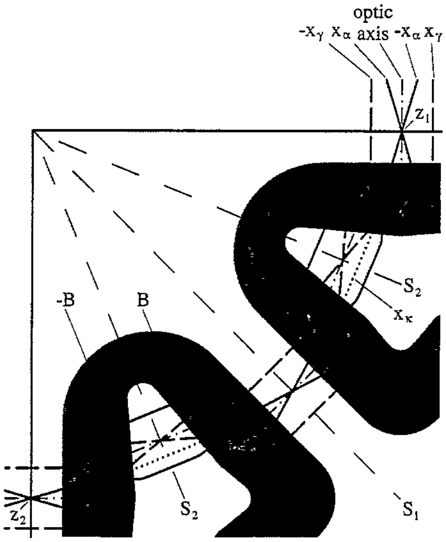

Fig. 6. Upper left quarter of the beam separator with the symmetry planes S_1 and S_2. The axial rays $\pm x_\alpha$, the field rays $\pm x_\gamma$ and the dispersion ray x_κ propagate in the midsection which is chosen as the x,z-plane of the curved x,y,z coordinate system.

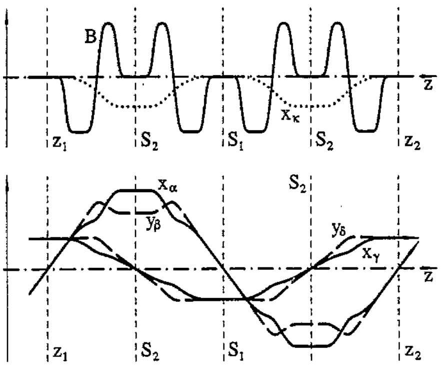

Fig. 7. The dipole field and the fundamental rays along the straightened optic axis.

The regions with non-vanishing dipole fields are shown in Fig. 6. They determine the meandering course of the optic axis. The path of the axial rays x_α, y_β and of the field rays x_γ, y_δ (see Fig. 7) are arranged in such a way that in the Gaussian approximation the entrance plane z_1 is imaged onto the exit plane z_2 with unit magnification. The dipole field, the optic axis and the fundamental rays are either point-symmetric or axially symmetric with respect to the plane S_1. This also holds true for the symmetry with respect to the plane S_2.

The distribution of the dipole field and the course of the fundamental rays x_α, y_β, x_γ, y_δ and x_κ along the straightened optic axis are depicted in Fig. 7. These functions are axially symmetric and point-symmetric about the planes S_1 and S_2, respectively. Owing to this double symmetry several second-rank deviations, which arise in the first half of the beam separator, are cancelled out in the second half. In particular, all geometric second-order deviations and the dispersions of first and second degree vanish after each 90° deflection, as shown in Fig. 8. In addition, several third-order aberrations are also eliminated. The image aberrations are defined as the values of the corresponding path deviations at the Gaussian image plane.

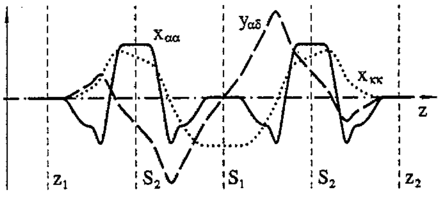

Fig. 8. The second-rank deviations $x_{\alpha\alpha}$, $y_{\alpha\delta}$ and $x_{\kappa\kappa}$ along the straightened optic axis. The deviations $x_{\alpha\alpha}$, $y_{\alpha\delta}$ and $x_{\kappa\kappa}$ at the final image plane produce axial coma, inclination of the image field and second-degree dispersion. Due to the twofold symmetry shown in Fig. 7 these deviations vanish in the region behind the exit plane z_2.

The highly symmetric design of the beam separator combines a 90° deflection with an imaging equivalent to that of a telescopic round lens doublet. Moreover, the finite dispersion at the planes S_2 offers the possibility to preselect the energy by inserting energy selection slits at these planes.

4.5.3. Tetrode mirror

To elucidate the properties of an electrostatic mirror we consider the simple diode mirror shown in Fig. 9. The equipotential surface $\varphi = 0$ has a concave shape in the paraxial region and a convex shape in the outer region. In addition, the path of an electron is shown which starts with zero velocity from a distinct position on this equipotential. An electron that enters the mirror along this path traverses it again after the reflection. Considering these properties, we can describe the action of the mirror by a simplified model. Electrons with a certain energy are reflected at the equipotential $\varphi = 0$ like light rays from the surface of a mirror. Accordingly, an electron which starts from the optic axis at a distance $z_i - z_m$ from the centre of the mirror returns to this point if the distance equals twice the focal length of the mirror (see Fig. 10(a)). An electron with a higher kinetic energy penetrates deeper into the mirror. At the turning point the curvature of the equipotential for $\varphi < 0$ is larger (see Figs 9 and 10(b)), resulting in stronger refraction.

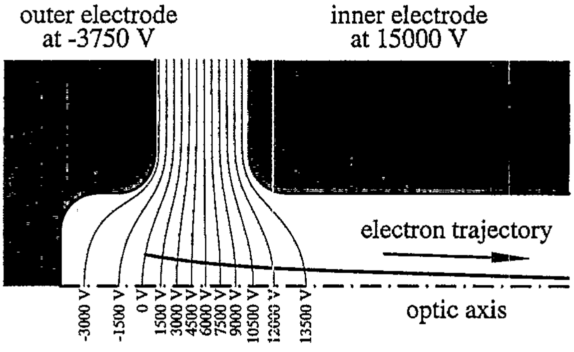

Fig. 9. Equipotentials of a simple, rotationally symmetric diode mirror. The depicted trajectory stems from an electron which starts with zero velocity from the equipotential $\varphi = 0$.

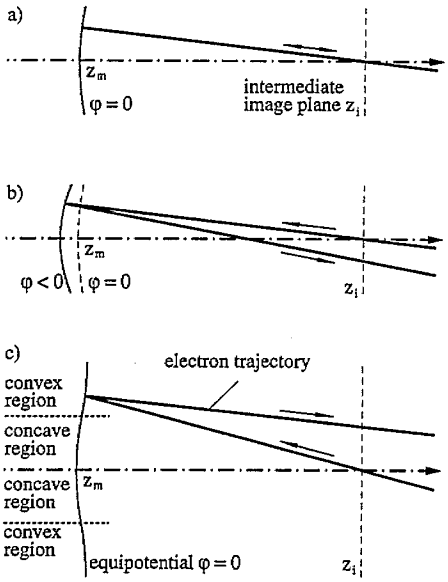

Fig. 10. Simplified model illustrating the properties of a concave–convex electron mirror: (a) the electron is reflected in the paraxial, concave region at the equipotential surface $\varphi = 0$ such that its incident trajectory coincides with the reflected trajectory; (b) the kinetic energy of the paraxial electron is increased, so that it is reflected by an equipotential $\varphi < 0$ with a locally stronger curvature; (c) a large initial angle results in a reflection within the convex region of the equipotential surface $\varphi = 0$.

An electron which starts from z_i with a large inclination reaches the equipotential $\varphi = 0$ at a position where its curvature is smaller than in the paraxial region, as demonstrated in Fig. 10(c). Hence this electron is less strongly focused than the paraxial electron.

The schematic paths of rays convincingly illustrate that concave–convex electron mirrors are able to correct the spherical and the chromatic aberrations of round lenses. The compensating aberrations of the mirror can be adjusted by means of two additional electrodes which properly shape the equipotential surfaces.

The electron mirror shown in Fig. 4 consists of four rotationally symmetric electrodes. The inner electrode is put at the constant column potential of 15 kV, while the potentials of the three other electrodes can be varied. They determine the focal length, the chromatic aberration and the spherical aberration of the mirror. For a fixed focal length these aberrations can be adjusted between zero and a maximum negative value which depends on the focal length and the geometrical dimensions of the mirror. This possibility enables one to correct the aberrations of the objective lens for different modes of operation, as demonstrated in Fig. 11.

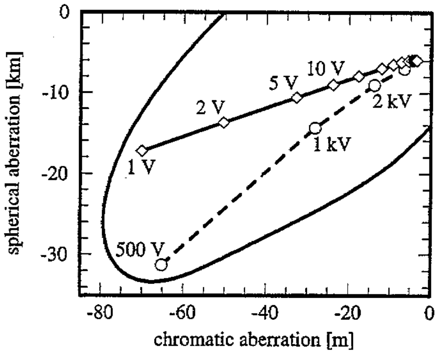

Fig. 11. Region of variation of the spherical and chromatic aberrations of a tetrode mirror with fixed focal length and the values required to correct the aberrations of the objective lens for different object potentials. The solid curve corresponds to a sample immersed in an electric field of 5 kV mm^{-1}; along the dashed curve the electric field is negligible.

4.5.4. Resolution improvement

Depending on the mode of operation of the objective lens, the correction of the primary axial aberrations improves the resolution up to a factor of 15. Simultaneously, the usable aperture angle and the contrast increase. This enhancement is mainly limited by the fifth-order spherical aberration and the energy dependence of the third-order spherical aberration, as

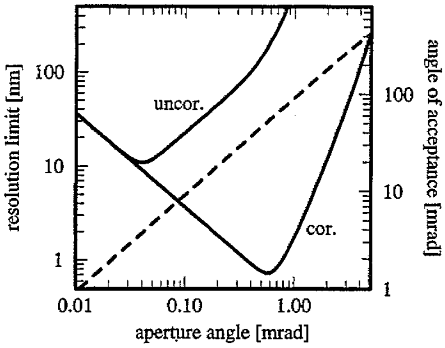

Fig. 12. Resolution limit and angle of acceptance in the case of a field-free object at 500 V. An energy window of ± 1 eV has been assumed for the energy filter. The solid lines represent the resolution limit as a function of the beam aperture at the entrance of the electron mirror for the corrected and uncorrected case; the dashed line describes the angle of acceptance in the object plane.

illustrated in Fig. 12 for the operation mode of a field-free object at 500 V. In the case of energy filtering with a narrow energy window only a very small fraction of the emitted electrons contributes to the image. Since this fraction is proportional to the square of the usable angle of acceptance (solid angle), the correction of the axial aberrations is very necessary in high-resolution core-level spectromicroscopy due to the low photoemission cross-sections and the radiation sensitivity of most samples.

4.6. Transfer optics

The transfer optics between the beam separator and the omega filter have to fulfil the following essential requirements. First, the intermediate images of object and source must be transferred to two fixed planes in front of the omega filter. It is important to note that the distance between these two planes, the Helmholtz length L, is a constant for any particular imaging energy filter regardless of the intermediate magnification at the filter. This constraint must therefore be satisfied for all modes of operation. The Helmholtz length of the omega filter chosen for the present instrument is $L = 95$ mm. Second, in order to record energy-filtered diffraction patterns instead of energy-filtered images, the location of the intermediate image in front of the omega filter has to be interchangeable with that of the intermediate source image. In the case of electron spectroscopic imaging, the transfer optics must cover a range of magnification M_T from 2 to 45, whereas in the electron spectroscopic diffraction mode the magnification M_T^D is about 2.

The transfer lens system shown in Fig. 13 consists of five electrostatic einzel lenses with the last two lenses forming a compound lens. The off-axial fundamental ray emerges from the beam separator with zero slope and intersects the optic axis midway between the first and second lens of the transfer optics. Hence an intermediate image of the source is located at this plane, $z = z_{Ap}$, where apertures of various diameter can be placed. In addition, the course of the axial fundamental ray is parallel to the optic axis in the region between the first and second einzel lens. To avoid readjustments of the aperture when changing the magnification, the electrode potential of the first lens is kept constant for all modes of operation. The paths of the fundamental rays through the transfer optics for a magnification of $M_T = 8$ are depicted in Fig. 13.

In order to facilitate the experimental operation of the transfer lens system, a design has been chosen that allows an almost independent adjustment of the intermediate images of object and source. The transfer optics itself will be operated in three different modes: (i) high-magnification imaging mode, (ii) low magnification imaging mode ($M_T = 2$) and (iii) diffraction mode. In the high-magnification imaging mode all five lenses are excited. In the low-magnification imaging mode and in the diffraction mode the fourth lens is switched off.

For a first rough design of the geometry of the

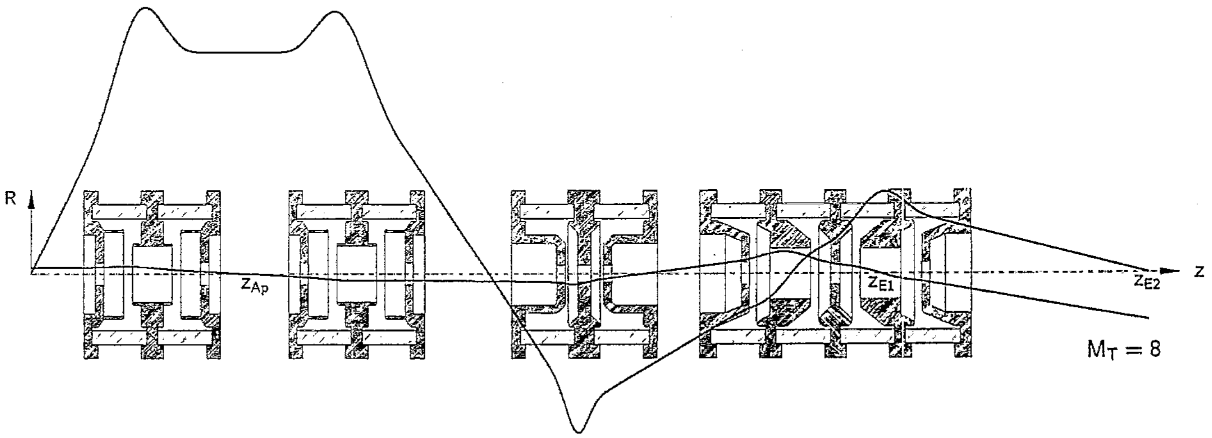

Fig. 13. Geometry of the transfer lens system consisting of five electrostatic einzel lenses and paths of the fundamental rays for a magnification $M_T = 8$.

individual electrodes the experimental data of Rempfer [35] have proven to be a very helpful guide. Rempfer measured the paraxial properties as well as the aberration coefficients of focal length and focal point for a wide range of electrostatic lens geometries. These data are in good agreement with our computations that are based on the charge density method [36]. Nevertheless, in order to meet all constraints imposed on the transfer lens system and to limit the aberrations of the transfer optics to an acceptable extent for all magnifications, an extensive optimization of the geometry of the individual electrodes had to be performed. A detailed analysis of the transfer lens system as a whole has shown that the third lens is the most critical one because it largely determines the total magnification of the transfer optics in the spectroscopic imaging mode.

Details of the calculation procedure and the optimization of the transfer lens system are described in [37]. The results demonstrate that the resolution and the number of image points determined by the corrected objective lens are not deteriorated by the transfer system because its primary aberrations are negligibly small.

4.7. Omega filter

The electron optics of imaging energy filters, particularly of the omega filter under consideration, have been described in detail from both the theoretical and the experimental points of view by Rose and Krahl [38]. The imaging energy filter for the present spectromicroscope under construction at the Fritz-Haber-Institut consists of four sector magnets, each deflecting the optic axis by 90°. Since the orientation of the magnetic dipole field within the first and fourth bending magnets is opposite to the orientation within the second and third, the optic axis resembles the Greek capital letter omega; hence, the name of the filter.

The omega filter possesses a mirror symmetry with respect to its midplane perpendicular to the optic axis. The first-order optical properties of the filter are defined by the deflection angle, the radius of curvature of the optic axis within the dipole fields, the tilt angles of the entrance and exit pole faces of the sector magnets and the distances between the individual magnets. These geometrical parameters are determined in such a way [20] that the first and second entrance planes in front of the filter are stigmatically imaged with unit magnification onto the energy dispersion plane and the achromatic image plane behind the filter, respectively, as schematically shown in Fig. 14. The two conjugate planes of each pair are located outside the filter and are arranged symmetrically with respect to its central plane. The symmetry becomes obvious in Fig. 15 where the paths of the fundamental rays are depicted along the straightened optic axis of the omega filter. The image plane $z = z_A$ is achromatic in the sense that all electrons are stigmatically focused onto this plane regardless of

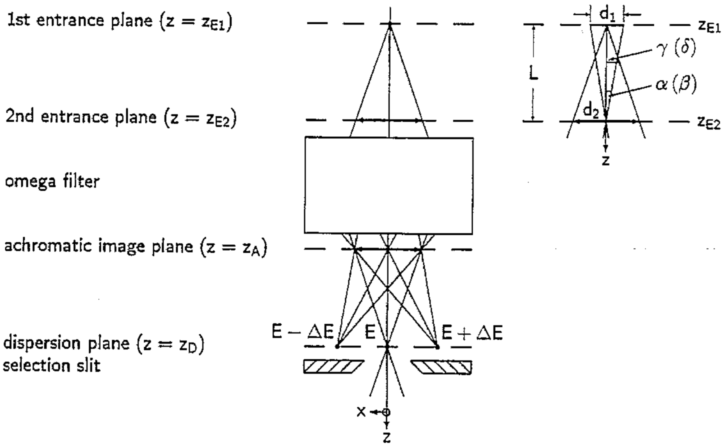

Fig. 14. Conjugate planes (z_{E1}, z_D) and (z_{E2}, z_A) for stigmatic focussing of the omega filter and definition of the ray parameters $\alpha(\beta)$ and $\gamma(\delta)$; d_1 defines the diameter of the source image and d_2 the diameter of the field of view in front of the energy filter; L is the Helmholtz length.

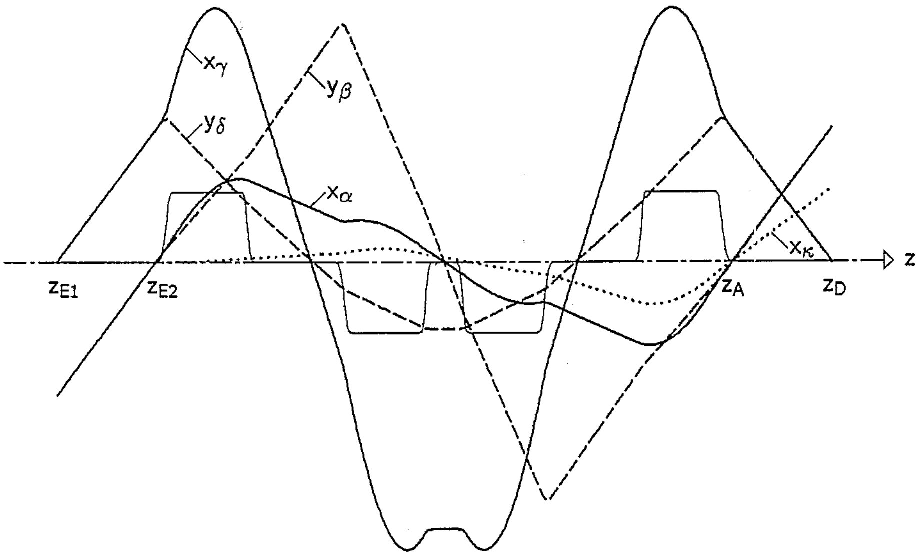

Fig. 15. Magnetic dipole field distribution and paths of the fundamental rays (x_α, y_β, x_γ, y_δ and x_κ) along the straightened optic axis of the omega filter.

their actual energy, because the (first-degree) spatial dispersion vanishes there. Nevertheless, due to the (first-degree) angular dispersion at this plane, electrons intersect the optic axis with different slopes depending on their energy. Detailed calculations of the geometry of the omega filter can be found in [39], in which particular attention was paid to the computation of the extended fringe fields of the sector magnets.

In the spectroscopic imaging mode of the microscope, an intermediate image of the source is located at the first entrance plane ($z = z_{\mathrm{E1}}$) and an intermediate image of the object at the second entrance plane ($z = z_{\mathrm{E2}}$). The achromatic image behind the filter is then magnified by the projector system onto the detector. The energy of the electrons can be selected by means of a slit placed near the dispersion plane where a diffraction pattern is located. Alternatively, in the spectrum mode of the microscope, the energy spectrum formed at the dispersion plane can be recorded by transferring this plane onto the image detector. For example, parallel recording of spectra within an energy band up to 35 eV should be possible at a resolution of 0.1 eV, as has already been mentioned in Section 3. For filtering diffraction patterns, the locations of the intermediate images of source and object in front of the energy filter are interchanged by appropriately adjusting the electrode potentials of the transfer lens system. Since the settings of the energy filter remain unchanged, the energy selection is again performed in the dispersion plane. This plane is, however, now conjugated to the object plane.

Magnetic energy filters possess 18 linearly independent second-rank aberration coefficients, as can be shown immediately by employing the eikonal method [40]. Ten coefficients determine the second-order (geometric) aberrations. Following the derivation given in [40,41], we distinguish between the coefficients $a_{\lambda\mu\nu}$ ($\lambda, \mu = \alpha, \gamma, \kappa$ and $\nu = \alpha,\gamma$), which only cause second-order deviations in the xz-section, and the coefficients $b_{\lambda\eta\sigma}$ ($\eta,\sigma = \beta,\delta$), which lead to second-order aberrations in both the xz- and the yz-sections. The other eight coefficients ($c_{\nu\xi\kappa}$, $c_{\nu\kappa\kappa}$, $c_{\rho\sigma\kappa}$; $\xi = \alpha,\gamma$) determine the second-rank chromatic aberrations. General integral expressions for the second-rank aberration coefficients and their classification in certain types of aberrations can be found in [40,41].

The second-rank aberrations at the (achromatic) image plane $z = z_{\mathrm{A}}$ of the omega filter have the form

$$\Delta x_A^{(2)} = -\left[\alpha^2 \boxed{a_{\alpha\alpha\alpha}} + \beta^2 \boxed{b_{\alpha\beta\beta}}/2 + 2\alpha\gamma \boxed{a_{\alpha\alpha\gamma}} + \beta\delta \boxed{b_{\alpha\beta\delta}} + \gamma^2 \boxed{a_{\alpha\gamma\gamma}} + \delta^2 \boxed{b_{\alpha\delta\delta}}/2 + \alpha\kappa\, c_{\alpha\alpha\kappa} + \gamma\kappa \boxed{c_{\alpha\gamma\kappa}} + \kappa^2\, c_{\alpha\kappa\kappa}\right] \qquad (1)$$

in the xz-section and

$$\Delta y_A^{(2)} = -\left[\alpha\beta\boxed{b_{\alpha\beta\beta}} + \alpha\delta\bbox[1px,border:1px dashed]{b_{\alpha\beta\delta}} + \beta\gamma\bbox[1px,border:1px dashed]{b_{\gamma\beta\beta}} + \gamma\delta\boxed{b_{\gamma\beta\delta}} + \beta\kappa\, c_{\beta\beta\kappa} + \delta\kappa\bbox[1px,border:1px dashed]{c_{\beta\delta\kappa}}\right] \tag{2}$$

in the yz-section. At the energy selection plane $z = z_D$ the second-rank aberrations are given by

$$\Delta x_D^{(2)} = \gamma^2\bbox[1px,border:1px dashed]{a_{\gamma\gamma\gamma}} + \delta^2\bbox[1px,border:1px dashed]{b_{\gamma\delta\delta}}/2 + 2\alpha\gamma\boxed{a_{\alpha\gamma\gamma}} + \beta\delta\boxed{b_{\gamma\beta\delta}} + \alpha^2\bbox[1px,border:1px dashed]{a_{\alpha\alpha\gamma}} + \beta^2\bbox[1px,border:1px dashed]{b_{\gamma\beta\beta}}/2 + \gamma\kappa\, c_{\gamma\gamma\kappa} + \alpha\kappa\bbox[1px,border:1px dashed]{c_{\alpha\gamma\kappa}} + \kappa^2\, c_{\gamma\kappa\kappa} \tag{3}$$

and

$$\Delta y_D^{(2)} = \gamma\delta\bbox[1px,border:1px dashed]{b_{\gamma\delta\delta}} + \gamma\beta\boxed{b_{\gamma\beta\delta}} + \alpha\delta\boxed{b_{\alpha\delta\delta}} + \alpha\beta\bbox[1px,border:1px dashed]{b_{\alpha\beta\delta}} + \delta\kappa\, c_{\delta\delta\kappa} + \beta\kappa\bbox[1px,border:1px dashed]{c_{\beta\delta\kappa}}\,, \tag{4}$$

respectively.

The geometrical ray parameters α, γ, β, δ and the aberration coefficients of the energy filter determine the aberrations. The geometrical ray parameters are connected with the components α_0, β_0 of the aperture angle at the object plane and the size $(2x_0, 2y_0)$ of the imaged area of the object via the relations

$$\alpha = \frac{\alpha_0}{M_i}\sqrt{\frac{\varphi_0}{\varphi}},\ \beta = \frac{\beta_0}{M_i}\sqrt{\frac{\varphi_0}{\varphi}},\ \gamma = \frac{x_0}{L}M_i \text{ and } \delta = \frac{y_0}{L}M_i \tag{5}$$

where M_i is the intermediate magnification at the omega filter. The energy parameter $\kappa = dE/E$ considers the energy deviation dE from the pass energy E. The sum of the exponents of the geometrical parameters α, β, γ and δ determines the order of the aberration and the exponent of the chromatic parameter κ its degree. The sum of order and degree defines, in our nomenclature, the rank of the aberration.

Due to the midplane symmetry of the omega filter, five second-order aberration coefficients vanish, since their contributions accumulated in the first half of the filter are compensated by corresponding negative contributions in the second half. The aberration coefficients cancelled by the symmetry conditions are framed with a solid box in eqns (1)–(4). The remaining five aberration coefficients, which are not eliminated by the midplane symmetry, can be corrected by means of seven additional sextupole elements symmetrically arranged about the central plane of the omega filter (see Fig. 1). The first and seventh sextupole are placed in front of and behind the filter near the planes $z = z_{E2}$ and $z = z_A$, respectively. Two sextupoles are located between the first and second sector magnet and two between the third and fourth. The fourth sextupole field is generated within a dodecapole element which also allows one to produce a quadrupole field. The dodecapole is placed at the central plane of the omega filter. The quadrupole field acts as a stigmator compensating for the astigmatism resulting from misalignment, mechanical inaccuracies or magnetic inhomogeneities of the sector magnets. In the spectroscopic imaging and diffraction mode all second-order (geometric) aberrations are cancelled as a result of the midplane symmetry of the omega filter and the seven appropriately excited sextupole elements.

The feasibility of this correction has already been demonstrated experimentally by Rose and Krahl [38]. The aberration coefficients, which are corrected in the spectroscopic imaging and diffraction mode by means of sextupoles, are indicated by dashed boxes in eqns (1)–(4). It should be noted that the chromatic aberration coefficients $c_{\alpha\gamma\kappa}$ and $c_{\beta\delta\kappa}$ vanish simultaneously if all second-order (geometrical) aberrations are corrected. Since the second-order aperture aberrations ($a_{\gamma\gamma\gamma}$, $b_{\gamma\delta\delta}$) are corrected, isochromatic energy filtering is possible without the need to reduce the ray parameters γ and δ which determine the field of view. Isochromatic energy filtering means that the selected energy does not depend on the position of the imaged object point. This property is mandatory for unambiguous elemental characterization.

The combined effect of the axial chromatic aberration and the dispersion is a tilt of the spectrum plane [38]. Accordingly, to avoid a blurring of the spectrum, the detector must either be tilted or the axial chromatic aberration must be corrected. The latter can be achieved by changing the settings of the sextupoles appropriately. Our calculations have shown that the axial chromatic aberration and the aperture aberration at the energy selection plane can be corrected simultaneously by readjusting three of the seven sextupole strengths.

Since all limiting second-rank aberrations can be corrected for any operation mode, the performance of the omega filter is primarily determined by the third-order aberrations. The obtainable energy resolution in the spectroscopy mode can be estimated from the spot size in the energy selection plane

$$\tilde{d}_\mathrm{D}=\sqrt{(d_\mathrm{D})^2+(\Delta x_\mathrm{D}^{(3)})^2} \tag{6}$$

where

$$d_D=2\alpha_0\sqrt{E_0/E}\cdot\frac{L}{M_\mathrm{i}} \tag{7}$$

is the size of the source image and

$$\Delta x_\mathrm{D}^{(3)}=2a_{\gamma\gamma\gamma\gamma}\left(\frac{d_0\cdot M_\mathrm{i}}{2L}\right)^3 \tag{8}$$

the dominating component of the third-order aberration.

In the spectroscopy mode, in which the second-order aperture aberration and the coefficient $c_{\gamma\gamma\kappa}$ are corrected, the dominating coefficient of the third-order aperture aberration adopts the value $a_{\gamma\gamma\gamma\gamma}$ = 39 m [42]. The diameter d_0 defines the imaged object area. The optimal intermediate magnification $M_\mathrm{i,opt}$ at the energy filter, which minimizes the spot size $\tilde{d}_\mathrm{D}$ is given by

$$M_\mathrm{i,\,opt}\approx 1.47\cdot L\cdot\left(\frac{\alpha_0\sqrt{E_0/E}}{d_0^3|a_{\gamma\gamma\gamma\gamma}|}\right)^{1/4} \tag{9}$$

Inserting $M_\mathrm{i,opt}$ into eqns (7) and (8) we obtain for the energy resolution

$$\delta E=\tilde{d}_\mathrm{D}/D\approx 1.58(\alpha_0 d_0)^{3/4}(E_0/E)^{3/8}|a_{\gamma\gamma\gamma\gamma}^{1/4}|/D \tag{10}$$

The dispersion of the omega filter $D = 35\ \mu\mathrm{m\ eV}^{-1}$ is quite large at an accelerating voltage U = 15 kV. In Table 2 the optimum parameters are listed for an energy resolution of δE = 0.1 eV. The corresponding aperture angles at the object plane $\alpha_0 = \alpha_{0,\mathrm{opt}}$ for optimum spatial resolution are taken from [43].

In the spectroscopic imaging or diffraction mode, energy filtering with an energy resolution of better than 0.1 eV can be performed if the diameter of the field aperture is smaller than 0.6 mm. This aperture is placed at the second entrance plane in front of the omega filter. A square grid can also be positioned in this plane and used to control the alignment of the filter as well as the position and excitation of the individual correction elements. In addition, it enables one to measure precisely the second-rank aberrations at the achromatic image plane and at the dispersion plane. The shadow image of the square grid enables a direct observation of the state of alignment obtained by successively adjusting the filter axis, the first-order and the second-order imaging properties. This extremely sensitive alignment procedure was developed by Rose and Krahl [38] and is an essential prerequisite for a successful operation of the omega filter.

Table 2

Optimum parameters α_0, d_0 and $M_\mathrm{i,opt}$ for different initial energies E_0 of the electrons in the case δE = 0.1 eV

E_0/eV	α_0/rad	d_0/μm	$M_\mathrm{i,opt}$
20	0.24	0.98	549
50	0.17	0.87	615
100	0.13	0.82	655
200	0.1	0.78	688

4.8. Projection system and image detector

The projector system consists of three electrostatic lenses which project either the sample image (diffraction pattern) at the achromatic image plane or the spectrum at the selection plane onto the image detector. In the first case, the magnification can be varied between 20 and 150. Thus the total magnification of the microscope can be chosen between about 5×10^2 and 10^5. The distortion, which is the only relevant third-order aberration introduced by the projector system, is less than 1% for all magnifications. Note that the first lens after the omega filter must be placed beyond the selection plane (see Fig. 1). Hence, this lens has a large focal length and transfers the image with a magnification of about 1 into the object plane of the second lens. The latter, together with the third lens, produces the magnification. In the second case—the spectroscopy mode—a line spectrum is produced by means of a quadrupole in order to increase the dynamic range detectable with a CCD detector, as has been described already in Section 3.3. The magnification can be set between 15 and 60 which is sufficient, on the one hand, to simultaneously record the transferable spectrum with a width of 35 eV and, on the other hand, to ensure that the energy resolution is not affected by the spatial resolution of the detector.

Two quickly interchangeable image detectors are planned as shown in Fig. 1. A TEM-1000n slow scan CCD camera and image acquisition system from Tietz Video and Image Processing Systems GmbH (Gauting, Germany) will be used for the recording of high-resolution images and spectra. A channel plate image intensifier combined with a TV-rate CCD camera comprises the second detector system that can be inserted for alignment purposes and for the observation of relatively fast processes at the sample surface.

5. Summary

By combining highly corrected electron optical components in a low-energy electron microscope with an optimized plane-grating monochromator on an undulator beamline, a versatile spectromicroscope called SMART has been designed for use at the BESSY II storage ring. This instrument will enable us to perform photoemission and X-ray absorption experiments in the soft X-ray range from 20 eV to about 1500 eV with spectroscopic and lateral resolutions well beyond the capabilities of existing instruments. A significant increase in lateral resolution is obtained by correction of the spherical and chromatic aberration of the objective lens of the microscope with an electrostatic tetrode mirror in combination with a highly symmetric magnetic beam separator. Theory predicts a lateral resolution below 1 nm, which may, however, be beyond the tolerance limits of stability and manufacturing precision of the various components. Nevertheless, we aim for a lateral resolution near 2 nm which is more than a factor 10 better than the performance of the best instruments built so far. Energy filtering of the electrons (photoelectrons, Auger electrons) is performed by a corrected omega filter with a maximum energy resolution of 0.1 eV. High spectral resolution in photoemission as well as in X-ray absorption experiments is possible due to the high spectral resolving power ($h\nu/\Delta h\nu > 10^4$) of the PM-6 monochromator, which has been optimized for a high photon flux of the order of 10^{10} photons μm^{-2}. In addition, the instrument will allow LEEM/MEM and small-area LEED studies using an additional electron source mounted at the beam separator.

For the first tests in 1998 the spectromicroscope will be operated with a UV lamp, probably without the beam separator. The high-resolution PM-6 plane grating monochromator is currently being installed at BESSY I and will be ready for operation in 1997. After the start of operation of BESSY II in 1998 the monochromator and the spectromicroscope will be moved to BESSY II and will be completed by the beam separator and the tetrode mirror.

Acknowledgements

We are deeply indebted to the late Helmut Petersen (BESSY) for his design of the PM-6 monochromator. We also thank the BESSY staff, in particular Professor W. Gudat (scientific director) and Dr Chr. Jung, for their support. The project is supported financially by the German Federal Ministry of Education and Research (BMBF) under contract no. 05 644 WWA 9. We are indebted to Dr L. Incoccia-Hermes and Mrs E. Thumann for their assistance in the project administration.

References

[1] L. Reimer (Ed.), Transmission electron microscopy, Springer Series in Optical Science, vol. 36, Berlin, 1993, and references cited therein.
[2] D. Briggs, M.P. Seah (Eds.), Practical Surface Analysis, vol. 1, Wiley, Chichester, 1990, and references cited therein.
[3] H. Ade, J. Kirz, S. Hulbert, E. Johnson, E. Anderson, D. Kern, Applied Physics Letters 56 (1990) 1841.
[4] G. Lilienkamp, Th. Schmidt, C. Koziol, E. Bauer, BESSY Annual Report, 1994, p. 469.
[5] E. Bauer, T. Franz, C. Koziol, G. Lilienkamp, T. Schmidt, in: R. Rosei (Ed.), Chemical, Structural and Electronic Analysis of Heterogenous Surfaces on the Nanometer Scale, Kluwer Academic, Dordrecht, in press.
[6] L.H. Veneklasen, Review of Scientific Instruments 63 (1992) 5513.
[7] G.R. Harp, B.P. Tonner, Review of Scientific Instruments 59 (1988) 852.

[8] J.D. Denlinger, E. Rotenberg, T. Warwick, G. Visser, J. Nordgren, J.-H. Guo, P. Skytt, S.D. Kevan, K.S. McCutcheon, D. Shuh, J. Bucher, N. Edelstein, J.G. Tobin, B.P. Tonner, Review of Scientific Instruments 66 (1995) 1342.

[9] B.P. Tonner, D. Dunham, T. Doubay, J. Kiuma, J. Denlinger, E. Rotenberg, A. Warwick, Journal of Electron Spectroscopy and Related Phenomena 75 (1995) 309.

[10] W. Engel, M.E. Kordesch, H.H. Rotermund, S. Kubala, A. von Oertzen, Ultramicroscopy 36 (1991) 148.

[11] F.U. Hillebrecht, T. Kinoshita, D. Spanke, J. Dresselhaus, Ch. Roth, H.B. Rose, E. Kisker, Physical Review Letters 75 (1995) 2224.

[12] J. Welnak, Z. Dong, H. Solak, J. Wallace, F. Cerrina, F. Bertolo, A. Bianco, S. Di Fronzo, S. Fontana, W. Jark, F. Mazzolini, R. Rosei, A. Savoia, J.H. Underwood, G. Margaritondo, Review of Scientific Instruments 66 (2) (1995) 2273.

[13] G. de Stasio, personal communication on the MEPHISTO project.

[14] Advanced Laboratory Source News 54 (1996).

[15] W.P. Skoczylas, G.F. Rempfer, O.H. Griffith, Ultramicroscopy 36 (1991) 252.

[16] G.F. Rempfer, M.S. Mauck, Optik 92 (1992) 3.

[17] G.F. Rempfer, D.M. Desloge, W.P. Skoczylas, O.H. Griffith, Microscopy and Microanalysis, (1997) in press.

[18] E. Bauer, Reports on Progress in Physics 52 (1994) 895.

[19] H. Rose, D. Preikszas, Optik 92 (1992) 31.

[20] S. Lanio, H. Rose, D. Krahl, Optik 73 (1986) 56.

[21] H.H. Rotermund, W. Engel, S. Jakubith, A. von Oertzen, G. Ertl, Ultramicroscopy 36 (1991) 164.

[22] R. Imbihl, G. Ertl, Chemical Review 95 (1995) 697.

[23] A. Garcia, M.E. Kordesch, Journal of Vacuum Science and Technology A 13 (1995) 1396.

[24] B. Rausenberger, W. Swiech, W. Engel, A.M. Bradshaw, E. Zeitler, Surface Science 288 (1993) 235.

[25] M. Snabl, M. Ondrejcek, V. Chab, W. Stenzel, H. Conrad, A.M. Bradshaw, Surface Science 352–354 (1996) 546.

[26] G.B. Birrell, K.K. Hedberg, D.L. Habliston, O.H. Griffith, Ultramicroscopy 36 (1991) 235.

[27] G.R. Harp, Z.-L. Han, B.P. Tonner, Journal of Vacuum Science and Technology A 8 (1990) 2566.

[28] W. Swiech, B. Rausenberger, W. Engel, A.M. Bradshaw, E. Zeitler, Surface Science 294 (1993) 297.

[29] E. Bauer, Ultramicroscopy 36 (1991) 52.

[30] Beamline Handbook, BESSY II, 1995.

[31] H. Petersen, Optics Communications 40 (1982) 402.

[32] M. Weiss, V. Wüstenhagen, R. Fink, E. Umbach, Journal of Electron Spectroscopy and Related Phenomena, this issue.

[33] O. Scherzer, Zeitschrift fuer Physik 101 (1936) 593.

[34] H. Rose, D. Preikszas, Nuclear Instruments & Methods A 363 (1995) 301.

[35] G.F. Rempfer, Journal of Applied Physics 57 (1985) 2385.

[36] E. Harting, F.H. Read, Electrostatic Lenses, Elsevier, Amsterdam, 1976.

[37] R. Degenhardt, W. Engel, in preparation.

[38] H. Rose, D. Krahl, in: L. Reimer (Ed.), Energy-filtering Transmission Electron Microscopy, Springer, Berlin, 1995, p. 43.

[39] S. Lanio, Dissertation D 17, Technische Hochschule, Darmstadt, Germany, 1986.

[40] H. Rose, Optik 51 (1978) 15.

[41] E. Plies, D. Typke, Zeitschrift fuer Naturforschung, Teil A 33 (1978) 1361.

[42] S. Uhlemann, H. Rose, Optik 96 (1994) 163.

[43] D. Preikszas, Dissertation D 17, Technische Hochschule, Darmstadt, Germany, 1995.